

CryoHype: Reconstructing a thousand cryo-EM structures with transformer-based hypernetworks

Jeffrey Gu^{1*}, Minkyu Jeon^{1*}, Ambri Ma¹, Serena Yeung-Levy², Ellen D. Zhong¹

¹Princeton University ²Stanford University

Abstract

Cryo-electron microscopy (cryo-EM) is an indispensable technique for determining the 3D structures of dynamic biomolecular complexes. While typically applied to image a single molecular species, cryo-EM has the potential for structure determination of many targets simultaneously in a high-throughput fashion. However, existing methods typically focus on modeling conformational heterogeneity within a single or a few structures and are not designed to resolve compositional heterogeneity arising from mixtures of many distinct molecular species. To address this challenge, we propose CryoHype, a transformer-based hypernetwork for cryo-EM reconstruction that dynamically adjusts the weights of an implicit neural representation. Using CryoHype, we achieve state-of-the-art results on a challenging benchmark dataset containing 100 structures. We further demonstrate that CryoHype scales to the reconstruction of 1,000 distinct structures from unlabeled cryo-EM images in the fixed-pose setting.

1. Introduction

Single particle cryo-electron microscopy (cryo-EM) has emerged as an essential tool to resolve the 3D structures of macromolecular complexes at atomic resolution [9, 33, 56]. Unlike static structure prediction algorithms or other structure determination methods, cryo-EM can experimentally probe the dynamic conformational states of large macromolecular complexes. However, 3D reconstruction of the resulting images poses a challenging inverse problem.

Although cryo-EM is typically used to resolve *conformational heterogeneity* within a single or a few structures from a purified sample, the technique is increasingly being used to capture more complex scenarios, including heterogeneous mixtures, unpurified samples, or cellular lysates [21, 22, 34, 42]. The ability to simultaneously resolve multiple distinct structures (*compositional heterogeneity*) presents a major opportunity for high-throughput structural discovery.

However, the complexity of these mixtures poses new modeling and inference challenges for cryo-EM reconstruction. In this work, we develop new architectures for modeling *extreme* compositional heterogeneity that can scale to datasets containing 10s-100s of distinct structures.

The standard approach for resolving discrete heterogeneity is 3D classification [15, 40, 45–47], a formulation that is naturally suited for modeling mixtures of distinct molecular species. While 3D classification models the dataset as originating from a discrete mixture of K independent voxel arrays, its reliance on Expectation-Maximization (EM) for inference limits its scalability to a small number of classes (typically $K < 10$). Because computational cost and memory requirements scale linearly with K , marginalization over class assignments (and optionally poses) becomes intractable for large values of K . Furthermore, in this regime, EM is highly sensitive to initialization and prone to optimization instability, often resulting in mode collapse and empty clusters.

In contrast, recent deep learning methods based on implicit or explicit neural representations [20, 24, 28, 29, 41, 57, 58] bypass the need for discrete classes by learning a continuous mapping from a continuous latent space to the volume density. While effective for modeling conformational heterogeneity, these methods are ill-suited for extreme compositional heterogeneity. Most architectures generate volumes using a fixed decoder conditioned on a latent vector. This design forces morphologically distinct structures to be represented by a single set of shared network weights. When applied to hundreds of distinct species, this excessive parameter sharing limits the model’s capacity to resolve high-frequency details for any individual structure.

Here, we introduce CryoHype, a transformer-based hypernetwork architecture designed to resolve extreme compositional heterogeneity. Using a hypernetwork [18] encoder allows the model to dynamically adapt the weights of the neural representation to each distinct structure, reducing parameter sharing and increasing expressivity compared to conditioning by concatenation [12, 32, 50]. The

*Equal contribution. JG completed the initial part of this work while at Stanford University.

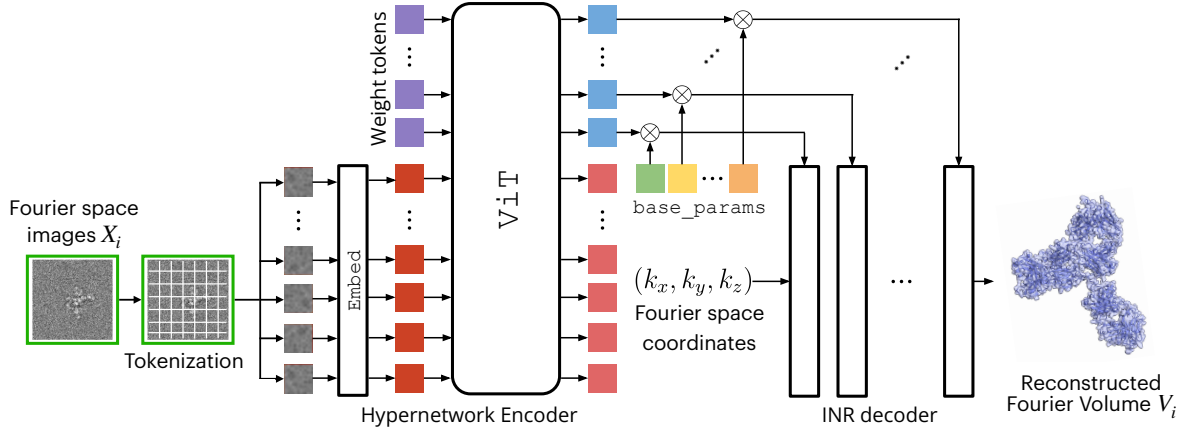


Figure 1. **CryoHype architecture.** An input image X_i of an unknown structure is first tokenized and concatenated with learnable weight tokens. All tokens are then processed with a transformer encoder, and the output weight tokens are used to modify the weights of an implicit neural representation (INR) that reconstructs the structure V_i .

vision transformer [11] (ViT) architecture for the hypernetwork provides scalable and parameter-efficient weight generation. In order to evaluate CryoHype, we introduce Sim2Struct-1000, a dataset for extreme compositional heterogeneity containing a mixture of 1,000 distinct structures, 10 times more structures than previous datasets for compositional heterogeneity [22]. Since traditional resolution-based metrics such as Fourier Shell Correlation (FSC) can be insensitive to variations in shape [13], we additionally evaluate our method using real-space 3D shape metrics. We demonstrate state-of-the-art performance with a 67% increase in FSC_{AUC} on the Tomotwin-100 dataset over the best baseline [22]. We further show that the hypernetwork architecture can scale to extreme compositional heterogeneity by reconstructing 1,000 unknown structures in the fixed-pose setting.

2. Methods

In this section, we introduce the cryo-EM image formation model (Section 2.1), motivation (Section 2.2), and our transformer-based hypernetwork method, CryoHype (Section 2.3).

2.1. Cryo-EM Image Formation Model

The cryo-EM reconstruction task is to recover structures $V_i : \mathbb{R}^3 \rightarrow \mathbb{R}, 1 \leq i \leq N$ of a set of noisy 2D projections X_1, \dots, X_N . In each projection X_i , the particle V_i is in an unknown pose ϕ_i , consisting of a rotation $R \in SO(3)$ and in-plane translation $t \in \mathbb{R}^2$. In Fourier space, the image formation model can be written as:

$$X_i = C_i \mathcal{P}(\phi_i) V_i + \epsilon \quad (1)$$

where C_i is the Contrast Transfer Function (CTF), \mathcal{P} is a slicing operator corresponding to projecting V_i at pose ϕ_i ,

and $\epsilon \sim \mathcal{N}(0, \sigma^2)$ models additive Gaussian noise. Additional details are provided in the Appendix.

2.2. Motivation

Previous neural volume representation methods in cryo-EM captured heterogeneity through either providing a latent code as additional input to an implicit neural representation (INR) volume representation [20, 27–29, 57] or as the coefficients of a linear combination of a shared basis of voxel arrays [24]. In either of these approaches, almost all parameters of the neural volume representations are shared among all the different structures, limiting the diversity of the structures that can be captured and the ability of the model to generate structure-specific high-resolution details. Hypernetworks overcome this problem by increasing the expressiveness of conditioning and reducing parameter sharing, since it can be proven that conditioning a network Ψ by concatenation is equivalent to having a linear hypernetwork produce the biases of the first layer of Ψ [12, 32, 50]. Two observations stem naturally from this result: first, that a general hypernetwork generalizes conditioning by concatenation and can be much more expressive if the hypernetwork is more expressive than a linear layer. Second, conditioning by concatenation is equivalent to sharing all hypernetwork (i.e. INR decoder) weights among all data points except its biases. Thus, hypernetwork approaches can dynamically adapt a significantly higher proportion of decoder weights than either conditioning-by-concatenation or linear combinations of voxel arrays.

2.3. CryoHype architecture

The CryoHype architecture consists of five main components: (1) a ViT encoder g , consisting of a tokenizer Embed and Transformer encoder Enc, (2) extra learnable weight

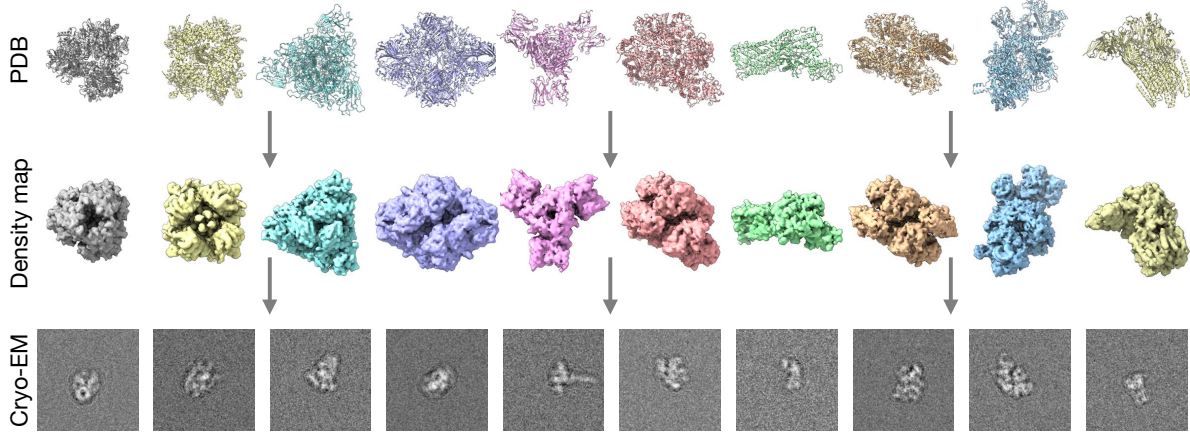


Figure 2. **Sim2Struct-1000**. Example atomic models, density maps, and projected images from Sim2Struct-1000, containing 1000 distinct structures.

tokens $\{w_i\}_{i=1}^q$ (3) an INR f , a ReLU MLP with residual connections, with a shared set of base parameters $\{\theta^i\}_{j=1}^L$ where L is the number of layers, and (4) learnable linear heads $\{\text{Head}_j\}_{j=1}^L$ for each layer L_j in f (see Figure 1). Reconstruction is done completely in the Fourier domain. A forward pass of our model works as follows: first, an input projection \hat{X} tokenized into T tokens $\{t_k\}_{k=1}^T$ by *Embed*. These T tokens are then concatenated along with the learnable weight tokens w_i and processed by *Enc*, the Transformer part of the ViT encoder, to produce the final tokens $[t_1^F, \dots, t_T^F, w_1^F, \dots, w_q^F]$. The output tokens corresponding to the weight tokens w_i^F are then divided into L groups consisting of a_j tokens $w_{a_1}^{F,j}, \dots, w_{a_j}^{F,j}, 1 \leq j \leq L$, with $\sum_i a_j = q$. The j th group $[w_{a_1}^{F,j}, \dots, w_{a_j}^{F,j}]$ is transformed by the linear head Head_j and normalized. The output of the previous step is multiplied elementwise by the j th layer’s base parameter θ_j to produce the final parameters θ_j^F of the j th layer::

$$\theta_j^F = \text{Norm}(\text{Head}_j([w_{a_1}^{F,j}, \dots, w_{a_j}^{F,j}])) \otimes \theta_j \quad (2)$$

Finally, the final INR parameters θ_i^F are used to instantiate the INR f , which parametrizes the structure \hat{V} . The INR f maps Fourier space coordinates (k_x, k_y, k_z) to the Fourier-transformed electron scattering potential at that coordinate, producing a clean (i.e., not noisy and CTF-free) prediction \tilde{X} . \tilde{X} is then multiplied by the CTF (see Section 2.1), and a reconstruction loss (mean-square error, MSE) is computed between the ground truth views and predicted views, and gradients are backpropagated to the hypernetwork. Note that CryoHype is trained end-to-end, with the learnable parameters being (1) the ViT encoder g , (2) the extra learnable weight tokens $w_i, 1 \leq i \leq q$, (3) the decoder’s base parameters $\theta_j, 1 \leq j \leq L$, where L is the number of layers in the decoder, and (4) the learnable linear heads $\text{Head}_j, 1 \leq j \leq L$.

Latent space embeddings. Unlike autoencoder and

autodecoder-based reconstruction methods, CryoHype does not have a canonical low-dimensional latent space. For our latent space analysis, we use the tokens w_1^F, \dots, w_q^F (blue tokens of Fig. 1). These tokens have total dimension qd where q is the number of weight tokens and d is the dimension of the ViT and are extremely high-dimensional. To obtain an interpretable latent space, we perform dimensionality reduction in two stages: first, we use principal component analysis (PCA) to reduce to a smaller dimension $d_1 \ll qd$, with $d_1 = 100$. We then use UMAP [31] to further reduce the dimension to 2 for visualization.

3. Experimental Settings

3.1. Datasets

We evaluate our method on two heterogeneous synthetic datasets containing extreme compositional heterogeneity: Tomotwin-100 [22] and our new challenging Sim2Struct-1000 dataset. We further demonstrate our method on an experimental dataset of the assembling ribosome [10].

CryoBench [22]. We evaluate on two synthetic datasets from CryoBench: IgG-1D and Tomotwin-100. The IgG-1D dataset simulates a 1D circular motion of a fragment antibody (Fab) domain of the human immunoglobulin G (IgG) antibody complex. IgG-1D is intended as a simple, diagnostic dataset and is used to validate our approach on conformational heterogeneity (latent space plots can be found in Appendix 13). Tomotwin-100 evaluates the capability of cryo-EM reconstruction algorithms to address extreme compositional heterogeneity. This dataset was generated by simulating the cryo-EM image formation process for 100 of the 120 distinct cellular complexes included in the TomoTwin dataset [43], curated to contain diverse and dissimilar proteins. Notably, Tomotwin-100 represents the most challenging dataset in [22], with most methods

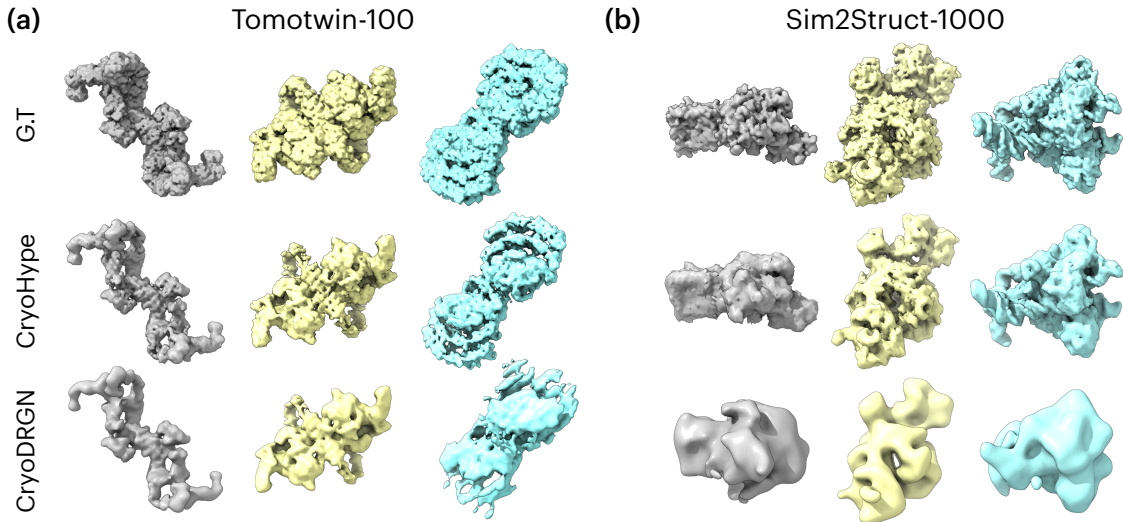


Figure 3. **Qualitative results of Tomotwin-100 and Sim2Struct-1000.** Representative density volumes and the corresponding ground truth volume. Additional examples are given in Figure 14 and Figure 15 in the Appendix.

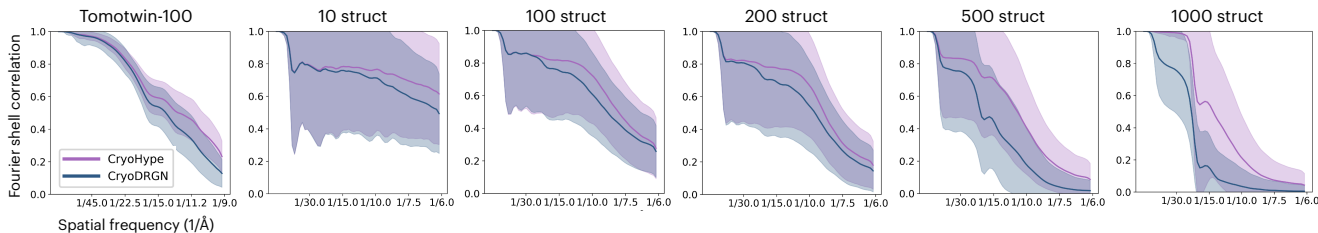


Figure 4. **Per-Image FSC.** Each curve shows the average FSC curve across all conformations with error bars indicating the standard deviation. The full FSC curves are shown in Appendix.

failing to achieve successful reconstructions.

Sim2Struct-1000. To evaluate model scalability to datasets containing a large degree of compositional heterogeneity, we introduce Sim2Struct-1000, a large-scale simulated cryo-EM dataset derived from the Cryo2StructData collection [14]. Cryo2StructData comprises experimentally obtained cryo-EM density maps paired with atomic models from the Protein Data Bank (PDB) [3]. Experimental cryo-EM maps from the original collection exhibited inconsistent resolution, noise levels, and grid dimensions due to diverse experimental parameters, potentially introducing confounding downstream biases. To avoid training models that learn these experimental settings, we instead selected a subset of 1000 atomic models filtered by particle size for Sim2Struct-1000. Each atomic model was converted to a density map and subsequently projected to create 1000 simulated images (256×256 , 3.0 Å/pix , downsampled to 128×128), resulting in a dataset of 1M total particle images (Figure 2). Sim2Struct-1000 thus allows evaluation of our method’s robustness under challenging conditions of compositional heterogeneity at scale. In our experiments, we examine four subsets of this dataset, representing differ-

ent amounts of compositional heterogeneity, consisting of 10, 100, 200, 500, and all 1000 structures. Each structure has 1000 simulated projection images. The complete details of Sim2Struct-1000’s construction can be found in Appendix 9.

EMPIAR-10076. We also evaluate our method on an experimental dataset, EMPIAR-10076 [10], which is known to exhibit significant compositional heterogeneity, comprising 14 discrete structures of the assembling 50S ribosome organized into four major assembly states. The data is pre-processed according to [58].

3.2. Metrics

We measure reconstruction quality with three metrics. The first, Fourier Shell Correlation (FSC), is a standard metric for comparing volumes in cryo-EM, computing correlation between Fourier shells at various thresholds and is a global measure of resolution, but can be misleading in the heterogeneous case [13]. We follow [22] and evaluate methods using the area under the FSC curve per image (FSC_{AUC}).

In addition, we propose two metrics from 3D shape analysis that measure reconstruction quality in real space and thus are more sensitive to local structural heterogeneity.

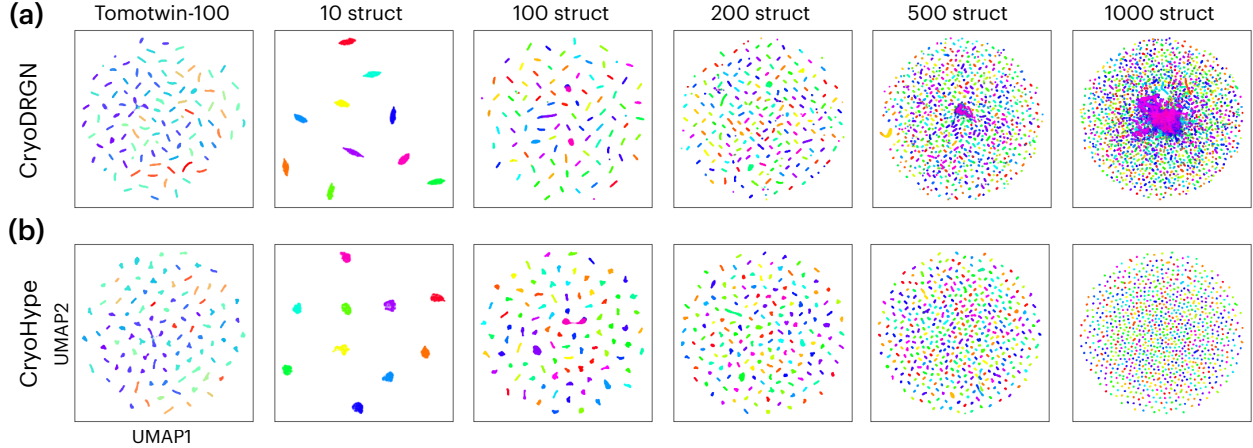


Figure 5. **Latent Visualization for Tomotwin-100 and Sim2Struct-1000.** (a) Latent embeddings from cryoDRGN visualized by UMAP and colored by the 10, 100, 200, 500, and 1000 G.T proteins. (b) Latent embeddings for CryoHype.

Table 1. **Quantitative performance on Tomotwin-100 (Noiseless)**, measured by FSC_{AUC} , CD, and vIoU. Metrics computed on back-projected images for each G.T. structure as an upper bound.

Method	Noiseless Tomotwin-100					
	\uparrow Mean FSC_{AUC} (std)	Median	\downarrow Mean CD (std)	Med	\uparrow Mean vIoU (std)	Med
CryoDRGN [58]	0.328 (0.022)	0.327	1.9750 (0.4450)	1.9165	0.6513 (0.0540)	0.6534
CryoHype	0.384 (0.019)	0.387	1.8663 (0.2514)	1.9002	0.6564 (0.0375)	0.6512
Backprojection	0.406 (0.018)	0.406	1.1931 (0.1987)	1.2130	0.7527 (0.0406)	0.7500

The first is volumetric intersection-over-union (IoU), which measures the volumetric overlap between volumes, and the second is Chamfer distance (CD), which captures pointwise differences between point clouds. We convert the voxel-based data to point clouds by extracting the coordinates of occupied voxels above a specified density threshold and scaling these to world coordinates based on voxel size and grid dimensions. Further analyses of our new metrics and details on the density threshold selection can be found in the Appendix.

3.3. Baselines

In Table 2, we examine a variety of state-of-the-art fixed-pose methods for cryo-EM reconstruction, including VAE-based reconstruction algorithms [24, 30, 58], autoencoder-based algorithms [29], and non-deep learning based algorithms [13, 38, 40]. For other experiments, we only compare against cryoDRGN [57, 58], the only baseline method that demonstrates reasonable performance in the case of extreme compositional heterogeneity (see Table 2 and [22]). CryoDRGN is a VAE whose decoder is a conditional implicit neural representation, conditioned by concatenation with the representation produced by the encoder.

4. Results

We conduct extensive experiments on synthetic and real-world datasets containing extreme compositional heterogeneity.

4.1. CryoBench

In noiseless Tomotwin-100, we find that CryoHype greatly outperforms CryoDRGN in FSC_{AUC} , approaching the performance of backprojection, and is better or comparable in all real space 3D shape metrics (Table 1). In the standard noisy (SNR 0.01) case, we note that all baselines except CryoDRGN are unable to handle extreme compositional heterogeneity and fail to produce reasonable reconstructions (Table 2). Here, we find that CryoHype clearly outperforms all baselines, including CryoDRGN, in the gold standard FSC_{AUC} metric. Compared to CryoDRGN, performance in 3D shape metrics is more mixed, which we attribute to the presence of minor artifacts in CryoHype’s reconstructions that are less prevalent in CryoDRGN’s reconstructions. Qualitatively, we find that CryoHype captures the global shape more precisely and more fine-grained details than CryoDRGN, resulting in higher resolution (Figure 3(a)), which is also reflected in the FSC curves (Figure 4). We attribute this to the more expressive conditioning of the CryoHype’s hypernetwork architecture. Both CryoHype and CryoDRGN produce reasonable looking latent

Table 2. **Quantitative performance on Tomotwin-100 (Noisy), measured by FSC_{AUC}, CD, and vIoU.** † results are from [22].

Method	Tomotwin-100					
	↑ Mean FSC _{AUC} (std)	Median	↓ Mean CD (std)	Med	↑ Mean vIoU (std)	Med
CryoDRGN [58]	0.316 (0.046) [†]	0.321 [†]	2.26 (1.59)	1.98	0.63 (0.08)	0.65
DRGN-AI-fixed [29]	0.202 (0.044) [†]	0.207 [†]	32.60 (18.45)	29.52	0.13 (0.09)	0.12
Opus-DSD [30]	0.237 (0.049) [†]	0.251 [†]	33.48 (0.1378)	28.92	0.14 (0.08)	0.13
SFBP [24]	0.036 (0.011)	0.036	18.52 (8.33)	17.32	0.16 (0.06)	0.16
3DVA [38]	0.088 (0.040) [†]	0.077 [†]	25.52 (17.90)	21.40	0.18 (0.09)	0.18
RECOVAR [13]	0.258 (0.109) [†]	0.254 [†]	27.22 (18.86)	23.14	0.16 (0.08)	0.15
3D Class [40]	0.046 (0.026) [†]	0.037 [†]	-	-	-	-
CryoHype	0.346 (0.033)	0.353	2.18 (0.46)	<u>2.11</u>	<u>0.61 (0.06)</u>	<u>0.62</u>
Backprojection	0.364 (0.023)	0.364	1.50 (0.20)	1.50	0.71 (0.03)	0.71

Table 3. **All Sim2Struct-1000 metrics.** Metrics are computed with standard deviations per method in parentheses. Chamfer distance is given in angstroms (Å). Isosurface levels are set at 220 for all subsets of Sim2Struct-1000.

Method	Structures	Sim2Struct-1000					
		↑ Mean FSC _{AUC} (std)	Median	↓ Mean CD (std)	Median	↑ Mean vIoU (std)	Median
CryoDRGN	10	0.434 (0.012)	0.437	1.9898 (0.3010)	2.0468	0.4853 (0.0524)	0.4806
CryoHype		0.464 (0.006)	0.465	1.7781 (0.1702)	1.7890	0.5005 (0.0336)	0.4939
CryoDRGN	100	0.361 (0.039)	0.357	2.3389 (0.6433)	2.2417	0.4731 (0.0602)	0.4664
CryoHype		0.409 (0.024)	0.407	1.9916 (0.4040)	1.9488	0.4897 (0.0516)	0.4849
CryoDRGN	200	0.334 (0.047)	0.334	2.4428 (1.0553)	2.2273	0.4765 (0.0673)	0.4766
CryoHype		0.377 (0.028)	0.375	2.0748 (0.3363)	2.0489	0.4726 (0.0484)	0.4697
CryoDRGN	500	0.216 (0.069)	0.213	4.6358 (4.2948)	3.1548	0.3866 (0.1293)	0.4101
CryoHype		0.305 (0.065)	0.322	2.4069 (0.7773)	2.2336	0.4529 (0.0773)	0.4565
CryoDRGN	1000	0.139 (0.054)	0.140	9.0656 (7.6560)	5.9439	0.2647 (0.1406)	0.2608
CryoHype		0.232 (0.079)	0.216	3.0179 (1.2470)	2.6512	0.4181 (0.1088)	0.4394

Table 4. Ablation study on CryoHype examining the four main components of the model, evaluated by FSC_{AUC}.

Method	Tomotwin-100	
	Mean (std)	Med
Concatenation	0.255 (0.076)	0.286
U-Net encoder	0.208 (0.031)	0.214
MLP encoder	0.234 (0.032)	0.240
CryoHype	0.346 (0.033)	0.353

spaces (Figure 5). CryoHype has much less variability, as indicated by smaller standard deviations for all metrics. We also find that higher FSCs do not necessarily result in higher Chamfer Distance or volumetric IoU, indicating that our new metrics are capturing differences in structure that are not being captured by FSC.

Diagnostic results on IgG-1D can be found in the Appendix 13. We find that although CryoHype was not specifically designed for conformational heterogeneity, it successfully recovers the circular motion of the IgG protein.

4.2. Sim2Struct-1000

Qualitatively, we find that CryoHype successfully reconstructs 1000 cryo-EM structures without any prior knowledge of the structures, while the best baseline (CryoDRGN) fails to reconstruct most details and even the correct shape. Quantitatively, we find that CryoHype significantly outperforms CryoDRGN at all levels of compositional heterogeneity (10, 100, 200, 500, and 1000 structures) in all metrics (Table 3). As shown by the FSC curves, CryoHype is higher resolution and captures all frequencies better than CryoDRGN across all levels of compositional heterogeneity (Figure 4). (Figure 3). CryoHype’s performance advantage over CryoDRGN increases as the compositional heterogeneity gets more extreme, showing the effect of INR parameter oversharing as heterogeneity increases. This trend is also reflected in the latent spaces (Figure 5). We find that while the latent spaces for both methods look well-clustered at lower levels of heterogeneity, the latent space of CryoDRGN starts to degrade at high levels of heterogeneity (500 structures and 1000 structure), indicating that CryoDRGN can no longer completely resolve the heterogeneity in the

dataset. In contrast, the latent space of CryoHype remains clustered by structure, even at the most extreme amounts of compositional heterogeneity.

4.3. Experimental compositional heterogeneity

Figure 6(a) illustrates reconstructed volumes of the four major classes of `EMPIAR-10076` produced by CryoHype and CryoDRGN. Due to the absence of ground truth volumes for experimental data, direct comparison of quality between the methods is challenging, however volumes are qualitatively similar. We additionally visualize the latent space colored by major and minor classes identified from the original publication (Fig. 6 (b)). Both methods successfully separate the major classes, and we note that CryoHype produces visually distinct clusters for minor assembly states as well (e.g., D1, D2, D3, and D4).

4.4. Ablation

In Table 4, we study the effectiveness of different components of our method by ablating the type of conditioning and the encoder architecture using `Tomotwin-100`. Hypernetwork conditioning greatly outperforms concatenation, which we attribute to its greater expressivity of (see Section 2.2). Changing the encoder from a transformer to a convolutional [44] or MLP [52] also results in heavily degraded performance despite the convolutional and MLP networks using more parameters, showing the importance of using a ViT encoder in hypernetwork architectures for parameter efficiency and scalability. Additional experiments comparing CryoHype against larger CryoDRGN variants as well full implementation details can be found in the Appendix.

5. Related Work

Cryo-EM heterogeneous reconstruction. Current methods for cryo-EM heterogeneous reconstruction can be broadly divided into non-neural and neural network-based approaches. 3D Classification [15, 40, 45–47] uses the Expectation-Maximization algorithm to sort images into a predefined number of discrete classes (typically < 10) and is highly sensitive to initialization. Non-neural methods for continuous heterogeneity typically use linear models for heterogeneity [2, 13, 38, 53]. 3DVA [38] and RECOVAR [13] are PCA-based methods that use probabilistic PCA and regularized covariance estimation, respectively. These methods learn a linear subspace describing structural heterogeneity, which may be limited in expressivity for diverse compositional heterogeneity settings [22].

Neural network-based methods typically operate entirely in Fourier space, leveraging the Fourier slice theorem [4] to avoid costly numerical integration. CryoDRGN [57] and its derivatives [27, 59] are variational autoencoder [25] (VAE)-based approaches that use MLP encoders and INR decoders,

respectively, while SFBP [24] is an autoencoder whose decoder is a linear combination of voxel arrays. OpusDSD [30] is another cryoDRGN-based VAE approach that uses a neural volume representation instead of an INR and incorporates a memory bank. Other methods instead represent volumes with Gaussian Mixture Models structure [7, 48]. 3DFlex [39], Hydra [28], and DRGN-AI [29] are encoder-free auto-decoder methods where each structure has a learnable latent code. These existing methods mainly focus on conformational heterogeneity with one or two different species and share almost all of their decoder weights among all reconstructed structures. In contrast, our method aims to model extreme compositional heterogeneity and reduces parameter sharing by dynamically adjusting the weights in every layer of the INR. Our work can also be interpreted as a generalization of discrete mixtures of neural fields [28] to a continuous mixture of neural fields.

Hypernetworks and INRs. A hypernetwork [18] is a neural network g_ϕ that produces or modifies the weights of another neural network f_θ , sometimes called the *primary network* or *hyponetwork*, typically an MLP, with the goal of learning the hypernetwork weights ϕ . This architecture allows the weights of the primary network to be dynamically adapted to different tasks. Most forms of INR conditioning are equivalent to having a hypernetwork producing a subset of its weights [55]. In particular, concatenation, the conditioning approach of most neural cryo-EM reconstruction methods, is equivalent to having an affine hypernetwork network that maps latent codes to the biases of the first layer of the hyponetwork [12, 32, 50]. In between the expressivity of full hypernetworks and concatenation are methods that predict feature-wise transformations [6, 12, 32], also called FiLM [36] conditioning, which predict a per-layer scale and bias. Our method uses a hypernetwork architecture that predicts the weights (but not the biases) of each layer, making it more expressive than conditioning by concatenation or FiLM. Hypernetworks that produce the weights of the primary network directly are difficult to train [35], so often the weights of the primary network are modified using a residual learning approach [8, 35]. Hypernetworks have been widely used to condition INRs [8, 16, 17, 23, 26, 49, 51, 52], especially generalizable INRs [8, 16, 17, 23, 26], where they outperform alternative methods of conditioning INRs such as gradient-based meta-learning [54]. Our insight is that these methods are designed to handle extreme compositional heterogeneity in shapes, with our method adapting [8] to the task of cryo-EM reconstruction.

Heterogeneous benchmarks for cryo-EM. The main heterogeneous benchmark for cryo-EM reconstruction is CryoBench [22], which proposes five new datasets with varying types of heterogeneity and degrees of difficulty. Among these, `Tomotwin-100` is the only CryoBench

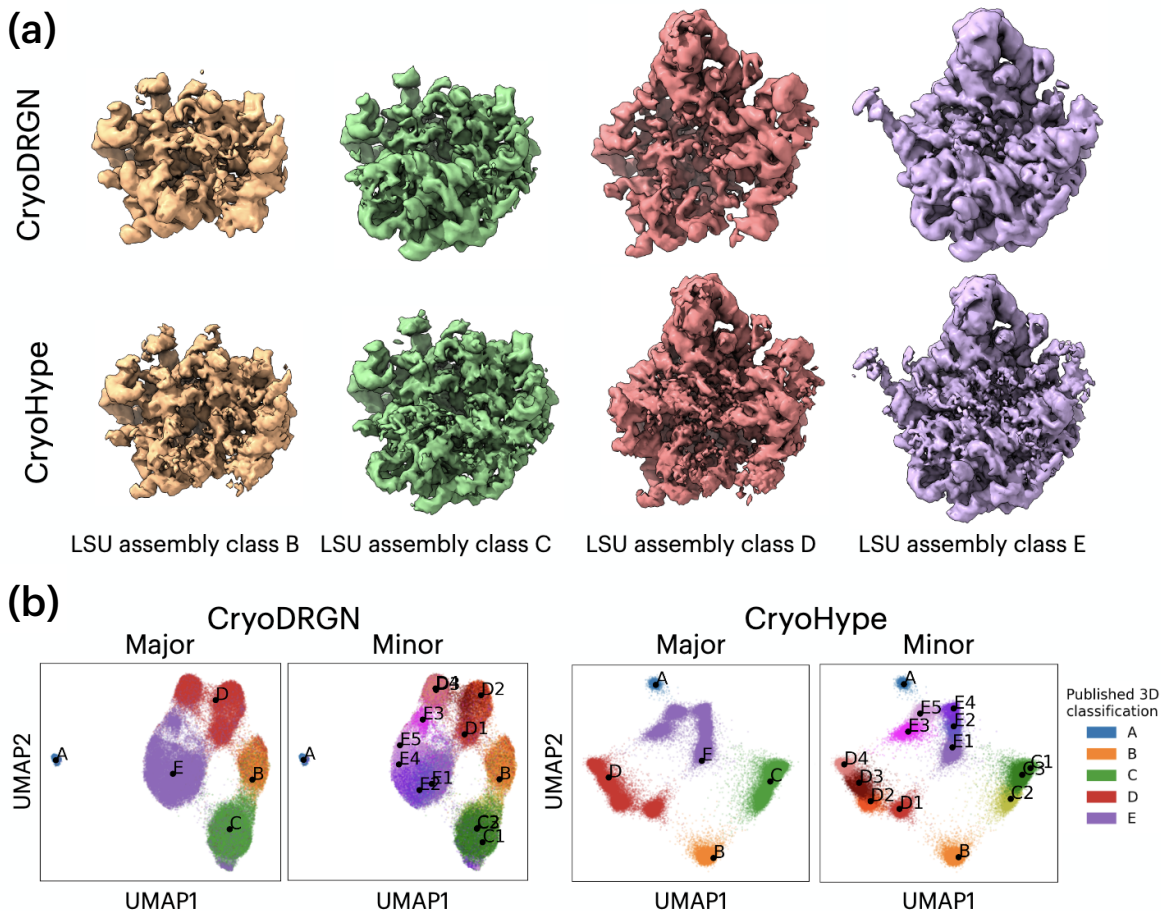


Figure 6. **Qualitative results on the EMPIAR-10076 dataset.** (a) Density maps of the four major ribosome assembly states from [10]. (b) Latent space representation, colored by major and minor assembly states assigned from the 3D classification in [10].

dataset that tackles extreme compositional heterogeneity with 100 distinct structures. We extend this further by proposing *Sim2Struct-1000*, a large-scale and challenging dataset for compositional heterogeneity derived from [14] that has 10 times as many structures as *Tomotwin-100*. Additionally, the standard volume-based metric for cryo-EM is Fourier shell correlation (FSC), which can be misleading for heterogeneous structures [13]. To provide a more complete evaluation of reconstruction quality, we propose two complementary real-space metrics that can capture heterogeneity missed by FSC.

6. Conclusion

We introduce CryoHype, a novel transformer hypernetwork approach that can reconstruct datasets with extreme compositional heterogeneity at high resolution. Across both synthetic and experimental datasets, we show that CryoHype more accurately recovers compositional heterogeneity from large-scale datasets over previous methods and produces more structured latent spaces. We also introduce

Sim2Struct-1000, a new dataset for compositional heterogeneity, as well as two complementary real-space metrics for evaluating cryo-EM reconstruction quality.

In this work, we focus on the architectural expressivity of hypernetworks for modeling extreme-scale compositional heterogeneity, and we note that CryoHype currently requires known particle poses. While this assumption is unrealistic in real experimental settings, it allows us to isolate and study the benefits of transformer-based hypernetwork conditioning. Extending CryoHype to *ab initio* reconstruction with joint pose estimation is an important next step, with natural integration into existing pose-search or amortized frameworks. Beyond pose inference, future work could investigate datasets containing both conformational and compositional heterogeneity, motion recovery within the latent space, and multi-view extensions such as tilt-series imaging. Together, these advances suggest that transformer-based hypernetworks, coupled with large-scale heterogeneous datasets, offer a foundation for developing computational methods to enable reconstructing diverse mixtures from cryo-EM at scale.

References

- [1] Josh Abramson, Jonas Adler, Jack Dunger, Richard Evans, Tim Green, Alexander Pritzel, Olaf Ronneberger, Lindsay Willmore, Andrew J. Ballard, Joshua Bambrick, Sebastian W. Bodenstein, David A. Evans, Chia-Chun Hung, Michael O'Neill, David Reiman, Kathryn Tunyasuvunakool, Zachary Wu, Akvilė Žemgulytė, Eirini Arvaniti, Charles Beattie, Ottavia Bertolli, Alex Bridgland, Alexey Cherepanov, Miles Congreve, Alexander I. Cowen-Rivers, Andrew Cowie, Michael Figurnov, Fabian B. Fuchs, Hannah Gladman, Rishub Jain, Yousuf A. Khan, Caroline M. R. Low, Kuba Perlin, Anna Potapenko, Pascal Savy, Sukhdeep Singh, Adrian Stecula, Ashok Thillaisundaram, Catherine Tong, Sergei Yakneen, Ellen D. Zhong, Michal Zielinski, Augustin Židek, Victor Bapst, Pushmeet Kohli, Max Jaderberg, Demis Hassabis, and John M. Jumper. Accurate structure prediction of biomolecular interactions with AlphaFold 3. *Nature*, 2024. 13
- [2] Joakim Andén and Amit Singer. Structural variability from noisy tomographic projections. *SIAM journal on imaging sciences*, 11(2):1441–1492, 2018. 7
- [3] Helen M Berman, John Westbrook, Zukang Feng, Gary Gilliland, Talapady N Bhat, Helge Weissig, Ilya N Shindyalov, and Philip E Bourne. The protein data bank. *Nucleic acids research*, 28(1):235–242, 2000. 4
- [4] Ronald N Bracewell. Strip integration in radio astronomy. *Australian Journal of Physics*, 9(2):198–217, 1956. 7, 12
- [5] Mateusz Buda, Ashirbani Saha, and Maciej A Mazurowski. Association of genomic subtypes of lower-grade gliomas with shape features automatically extracted by a deep learning algorithm. *Computers in biology and medicine*, 109:218–225, 2019. 16
- [6] Eric R Chan, Marco Monteiro, Petr Kellnhofer, Jiajun Wu, and Gordon Wetzstein. pi-gan: Periodic implicit generative adversarial networks for 3d-aware image synthesis. In *Proceedings of the IEEE/CVF conference on computer vision and pattern recognition*, pages 5799–5809, 2021. 7
- [7] Muyuan Chen and Steven J Ludtke. Deep learning-based mixed-dimensional gaussian mixture model for characterizing variability in cryo-em. *Nature methods*, 18(8):930–936, 2021. 7
- [8] Yinbo Chen and Xiaolong Wang. Transformers as meta-learners for implicit neural representations. In *European Conference on Computer Vision*, pages 170–187. Springer, 2022. 7
- [9] Yifan Cheng. Single-particle cryo-em—how did it get here and where will it go. *Science*, 361(6405):876–880, 2018. 1
- [10] Joseph H Davis, Yong Zi Tan, Bridget Carragher, Clinton S Potter, Dmitry Lyumkis, and James R Williamson. Modular assembly of the bacterial large ribosomal subunit. *Cell*, 167(6):1610–1622, 2016. 3, 4, 8, 19
- [11] Alexey Dosovitskiy. An image is worth 16x16 words: Transformers for image recognition at scale. *arXiv preprint arXiv:2010.11929*, 2020. 2
- [12] Vincent Dumoulin, Ethan Perez, Nathan Schucher, Florian Strub, Harm de Vries, Aaron Courville, and Yoshua Bengio. Feature-wise transformations. *Distill*, 3(7):e11, 2018. 1, 2, 7
- [13] Marc Aurèle Gilles and Amit Singer. Cryo-em heterogeneity analysis using regularized covariance estimation and kernel regression. *Proceedings of the National Academy of Sciences*, 122(9):e2419140122, 2025. 2, 4, 5, 6, 7, 8
- [14] Nandhini Giri, Limin Wang, and Jianlin Cheng. Cryo2structdata: A large labeled cryo-em density map dataset for ai-based modeling of protein structures. *Scientific Data*, 11(1):458, 2024. 4, 8, 12, 13
- [15] Timothy Grant, Alexis Rohou, and Nikolaus Grigorieff. cis tem, user-friendly software for single-particle image processing. *elife*, 7:e35383, 2018. 1, 7
- [16] Jeffrey Gu and Serena Yeung-Levy. Foundation models secretly understand neural network weights: Enhancing hypernetwork architectures with foundation models. *arXiv preprint arXiv:2503.00838*, 2025. 7
- [17] Jeffrey Gu, Kuan-Chieh Wang, and Serena Yeung. Generalizable neural fields as partially observed neural processes. In *Proceedings of the IEEE/CVF International Conference on Computer Vision*, pages 5330–5339, 2023. 7
- [18] David Ha, Andrew Dai, and Quoc V Le. Hypernetworks. *arXiv preprint arXiv:1609.09106*, 2016. 1, 7
- [19] Dan Hendrycks and Kevin Gimpel. Gaussian error linear units (gelus). *arXiv preprint arXiv:1606.08415*, 2016. 12
- [20] David Herreros, Carlos Perez Mata, Chari Noddings, Deli Irene, James Krieger, David A Agard, Ming-Daw Tsai, Carlos Oscar Sanchez Sorzano, and Jose Maria Carazo. Real-space heterogeneous reconstruction, refinement, and disentanglement of cryoem conformational states with hetsiren. *Nature communications*, 16(1):3751, 2025. 1, 2
- [21] Chi-Min Ho, Xiaorun Li, Mason Lai, Thomas C Terwilliger, Josh R Beck, James Wohlschlegel, Daniel E Goldberg, Anthony WP Fitzpatrick, and Z Hong Zhou. Bottom-up structural proteomics: cryoem of protein complexes enriched from the cellular milieu. *Nature methods*, 17(1):79–85, 2020. 1
- [22] Minkyu Jeon, Rishwanth Raghu, Miro Astore, Geoffrey Woollard, Ryan Feathers, Alkin Kaz, Sonya M Hanson, Pilar Cossio, and Ellen D Zhong. Cryobench: Diverse and challenging datasets for the heterogeneity problem in cryo-em. *arXiv preprint arXiv:2408.05526*, 2024. 1, 2, 3, 4, 5, 6, 7, 12, 13, 15, 18, 19
- [23] Chiheon Kim, Doyup Lee, Saehoon Kim, Minsu Cho, and Wook-Shin Han. Generalizable implicit neural representations via instance pattern composers. In *Proceedings of the IEEE/CVF Conference on Computer Vision and Pattern Recognition*, pages 11808–11817, 2023. 7
- [24] Dari Kimanius, Kiarash Jamali, and Sjors Scheres. Sparse fourier backpropagation in cryo-em reconstruction. *Advances in Neural Information Processing Systems*, 35:12395–12408, 2022. 1, 2, 5, 6, 7
- [25] Diederik P Kingma. Auto-encoding variational bayes. *arXiv preprint arXiv:1312.6114*, 2013. 7
- [26] Doyup Lee, Chiheon Kim, Minsu Cho, and WOOK SHIN HAN. Locality-aware generalizable implicit neural representation. *Advances in Neural Information Processing Systems*, 36, 2024. 7

- [27] Axel Levy, Gordon Wetzstein, Julien NP Martel, Frederic Poitevin, and Ellen Zhong. Amortized inference for heterogeneous reconstruction in cryo-em. *Advances in neural information processing systems*, 35:13038–13049, 2022. 2, 7
- [28] Axel Levy, Rishwanth Raghu, David Shustin, Adele Peng, Huan Li, Oliver Clarke, Gordon Wetzstein, and Ellen Zhong. Mixture of neural fields for heterogeneous reconstruction in cryo-em. *Advances in Neural Information Processing Systems*, 37:56988–57017, 2024. 1, 7
- [29] Axel Levy, Rishwanth Raghu, J Ryan Feathers, Michal Grzadkowski, Frédéric Poitevin, Jake D Johnston, Francesca Vallese, Oliver Biggs Clarke, Gordon Wetzstein, and Ellen D Zhong. Cryodrgn-ai: neural ab initio reconstruction of challenging cryo-em and cryo-et datasets. *Nature Methods*, pages 1–9, 2025. 1, 2, 5, 6, 7
- [30] Zhenwei Luo, Fengyun Ni, Qinghua Wang, and Jianpeng Ma. Opus-dsd: deep structural disentanglement for cryo-em single-particle analysis. *Nature Methods*, 20(11):1729–1738, 2023. 5, 6, 7
- [31] Leland McInnes, John Healy, and James Melville. Umap: Uniform manifold approximation and projection for dimension reduction. *arXiv preprint arXiv:1802.03426*, 2018. 3
- [32] Ishit Mehta, Michaël Gharbi, Connelly Barnes, Eli Shechtman, Ravi Ramamoorthi, and Manmohan Chandraker. Modulated periodic activations for generalizable local functional representations. In *Proceedings of the IEEE/CVF International Conference on Computer Vision*, pages 14214–14223, 2021. 1, 2, 7
- [33] Takanori Nakane, Dari Kimanius, Erik Lindahl, and Sjors HW Scheres. Characterisation of molecular motions in cryo-em single-particle data by multi-body refinement in relion. *elife*, 7:e36861, 2018. 1
- [34] Eva Nogales and Julia Mahamid. Bridging structural and cell biology with cryo-electron microscopy. *Nature*, 628(8006):47–56, 2024. 1
- [35] Jose Javier Gonzalez Ortiz, John Guttag, and Adrian Dalca. Magnitude invariant parametrizations improve hypernetwork learning. *arXiv preprint arXiv:2304.07645*, 2023. 7
- [36] Ethan Perez, Florian Strub, Harm De Vries, Vincent Dumoulin, and Aaron Courville. Film: Visual reasoning with a general conditioning layer. In *Proceedings of the AAAI conference on artificial intelligence*, 2018. 7
- [37] Eric F Pettersen, Thomas D Goddard, Conrad C Huang, Elaine C Meng, Gregory S Couch, Tristan I Croll, John H Morris, and Thomas E Ferrin. Ucsf chimeraX: Structure visualization for researchers, educators, and developers. *Protein Science*, 2021. 15
- [38] Ali Punjani and David J Fleet. 3d variability analysis: Resolving continuous flexibility and discrete heterogeneity from single particle cryo-em. *Journal of structural biology*, 213(2):107702, 2021. 5, 6, 7
- [39] Ali Punjani and David J Fleet. 3dflex: determining structure and motion of flexible proteins from cryo-em. *Nature Methods*, 20(6):860–870, 2023. 7
- [40] Ali Punjani, John L Rubinstein, David J Fleet, and Marcus A Brubaker. cryosparc: algorithms for rapid unsupervised cryo-em structure determination. *Nature methods*, 14(3):290–296, 2017. 1, 5, 6, 7, 18
- [41] Huaizhi Qu, Xiao Wang, Yuanyuan Zhang, Sheng Wang, William Stafford Noble, and Tianlong Chen. Cryonerf: reconstruction of homogeneous and heterogeneous cryo-em structures using neural radiance field. *bioRxiv*, pages 2025–01, 2025. 1
- [42] Jessica N Rabuck-Gibbons, Dmitry Lyumkis, and James R Williamson. Quantitative mining of compositional heterogeneity in cryo-em datasets of ribosome assembly intermediates. *Structure*, 30(4):498–509, 2022. 1
- [43] Gavin Rice, Thorsten Wagner, Markus Stabrin, Oleg Sitsel, Daniel Prumbaum, and Stefan Raunser. Tomotwin: generalized 3d localization of macromolecules in cryo-electron tomograms with structural data mining. *Nature methods*, 20(6):871–880, 2023. 3
- [44] Olaf Ronneberger, Philipp Fischer, and Thomas Brox. U-net: Convolutional networks for biomedical image segmentation. In *Medical image computing and computer-assisted intervention—MICCAI 2015: 18th international conference, Munich, Germany, October 5–9, 2015, proceedings, part III 18*, pages 234–241. Springer, 2015. 7, 16
- [45] Sjors HW Scheres. Relion: implementation of a bayesian approach to cryo-em structure determination. *Journal of structural biology*, 180(3):519–530, 2012. 1, 7
- [46] Sjors HW Scheres. Processing of structurally heterogeneous cryo-em data in relion. *Methods in enzymology*, 579:125–157, 2016.
- [47] Sjors HW Scheres, Haixiao Gao, Mikel Valle, Gabor T Herman, Paul PB Eggermont, Joachim Frank, and Jose-Maria Carazo. Disentangling conformational states of macromolecules in 3d-em through likelihood optimization. *Nature methods*, 4(1):27–29, 2007. 1, 7
- [48] Johannes Schwab, Dari Kimanius, Alister Burt, Tom Den-doooven, and Sjors HW Scheres. Dynamight: estimating molecular motions with improved reconstruction from cryo-em images. *Nature Methods*, 21(10):1855–1862, 2024. 7
- [49] Vincent Sitzmann, Michael Zollhöfer, and Gordon Wetzstein. Scene representation networks: Continuous 3d-structure-aware neural scene representations. *Advances in Neural Information Processing Systems*, 32, 2019. 7
- [50] Vincent Sitzmann, Eric Chan, Richard Tucker, Noah Snively, and Gordon Wetzstein. Metasdf: Meta-learning signed distance functions. *Advances in Neural Information Processing Systems*, 33:10136–10147, 2020. 1, 2, 7
- [51] Vincent Sitzmann, Julien Martel, Alexander Bergman, David Lindell, and Gordon Wetzstein. Implicit neural representations with periodic activation functions. *Advances in neural information processing systems*, 33:7462–7473, 2020. 7
- [52] Vincent Sitzmann, Semon Rezchikov, Bill Freeman, Josh Tenenbaum, and Fredo Durand. Light field networks: Neural scene representations with single-evaluation rendering. *Advances in Neural Information Processing Systems*, 34:19313–19325, 2021. 7, 18
- [53] Hemant D Tagare, Alp Kucukelbir, Fred J Sigworth, Hongwei Wang, and Murali Rao. Directly reconstructing principal components of heterogeneous particles from cryo-em images. *Journal of structural biology*, 191(2):245–262, 2015. 7

- [54] Matthew Tancik, Ben Mildenhall, Terrance Wang, Divi Schmidt, Pratul P Srinivasan, Jonathan T Barron, and Ren Ng. Learned initializations for optimizing coordinate-based neural representations. In *Proceedings of the IEEE/CVF Conference on Computer Vision and Pattern Recognition*, pages 2846–2855, 2021. [7](#)
- [55] Yiheng Xie, Towaki Takikawa, Shunsuke Saito, Or Litany, Shiqin Yan, Numair Khan, Federico Tombari, James Tompkin, Vincent Sitzmann, and Srinath Sridhar. Neural fields in visual computing and beyond. In *Computer Graphics Forum*, pages 641–676. Wiley Online Library, 2022. [7](#)
- [56] Ka Man Yip, Niels Fischer, Elham Paknia, Ashwin Chari, and Holger Stark. Atomic-resolution protein structure determination by cryo-em. *Nature*, 587(7832):157–161, 2020. [1](#)
- [57] Ellen D Zhong, Tristan Bepler, Joseph H Davis, and Bonnie Berger. Reconstructing continuous distributions of 3d protein structure from cryo-em images. In *International Conference on Learning Representations*, 2020. [1](#), [2](#), [5](#), [7](#)
- [58] Ellen D Zhong, Tristan Bepler, Bonnie Berger, and Joseph H Davis. Cryodrgn: reconstruction of heterogeneous cryo-em structures using neural networks. *Nature methods*, 18(2): 176–185, 2021. [1](#), [4](#), [5](#), [6](#), [12](#), [15](#), [16](#), [18](#)
- [59] Ellen D Zhong, Adam Lerer, Joseph H Davis, and Bonnie Berger. Cryodrgn2: Ab initio neural reconstruction of 3d protein structures from real cryo-em images. In *Proceedings of the IEEE/CVF International Conference on Computer Vision*, pages 4066–4075, 2021. [7](#)

7. Cryo-EM image formation model

In this section, we expand on Section 2.1. Recall that the real space image formation model is given by Equation 1, and that this formulation is generally not used as a forward map during training due to the cost of computing the integral. Instead, most reconstruction methods exploit the Fourier Slice Theorem (FST) [4] to simulate the image formation model efficiently in Fourier space. The FST states that the Fourier transform of a 2D projection of V is a 2D slice through the origin of V of the 3D Fourier transform of V , which simplifies the image formation model by circumventing the need to compute the integral. Using the FST, we can write the image formation model in Fourier space as

$$\hat{X}(k_x, k_y) = \hat{g}T(t)S(R)\hat{V}(k_x, k_y) + \hat{\epsilon} \quad (3)$$

where $\hat{g} = \mathcal{F}g$ is the contrast-transfer function (CTF) of the microscope, and T and S are translation and slice operators corresponding to translation in the real space and rotation and then projection in the real space, respectively. The Fourier domain noise $\hat{\epsilon}$ is usually modeled as independent, zero-mean Gaussian noise, which is what we do in this paper.

8. Architecture and training details

Here, we provide the architecture and training details of our experiments.

Transformer encoder architecture For the Tomotwin-100 experiment, our transformer encoder consists of six transformer blocks, with each block consisting of a multi-head self-attention layer followed by an MLP consisting of two linear layers with GeLU activations [19]. Each MHSA layer consisted of 12 heads with each head having dimension 64, with the total dimension being 768. The hidden dimension of each MLP is 3072. The Transformer encoder used for the Sim2Struct-1000 experiments were identical except eight blocks were used instead of six.

INR decoder architecture For all experiments, we used an INR consisting of 5 layers with hidden dimension 1024, random Fourier feature positional encoding, and residual connections between each layer. For fair comparison, we used this INR architecture for both CryoHype and baseline models.

Training hyperparameters The Tomotwin-100 experiment was carried out with a batch size of 64, learning rate of $1e-4$, a cosine learning rate schedule with a linear warmup of 5 epochs, patch size of 16, and was

trained for a total of 50 epochs. For the 10 structure subset of Sim2Struct-1000, we used a learning rate of $5e-4$, while for experiments with more structures, we used a learning rate of $2e-4$, with all other hyperparameters being the same as the Tomotwin-100 experiment. Finally, for the EMPIAR-10076, we used a patch size of 4 with a Gaussian low-pass filter cutoff of 50. A Gaussian low-pass filter is applied to each input token for the Vision Transformer (ViT), with all other hyperparameters being the same as the Tomotwin-100 experiment. All hyperparameters were tuned using grid search.

CryoDRGN We trained CryoDRGN using the official PyTorch implementation¹ (version 3.4.0b). For the synthetic datasets, all results were obtained using the default settings, with the z-dimension set to 8 and the total number of training epochs is 20 as described in [22]. For experiments on Sim2Struct-1000, we used a batch size of 64 and 50 training epochs. For experiments on EMPIAR-10076, we followed the settings outlined in [58], using 50 training epochs with the latent z-dimension set to 10.

Training splits As is standard for cryo-EM reconstruction, for all datasets we did not split any of the datasets and used the entire dataset for training. Datasets from CryoBench [22], including Tomotwin-100, can be downloaded from Zenodo.

GPUs, Memory, and Compute Time Model were trained on either NVIDIA A100, NVIDIA V100, NVIDIA A6000 GPU, or NVIDIA L40S GPUs. Each model were trained using 2 GPUs using PyTorch Lightning. Training a CryoHype model for 50 epochs and performing inference took approximately 8 hours on 2 A100 GPUs for a dataset with 100K total particles (e.g. Tomotwin-100 or the 100 structure subset of Sim2Struct-1000). A dataset of this size uses 77.7GB CPU memory and uses 24.5GB VRAM for a batch size of 32. For larger datasets, CPU memory consumption can be reduced using lazy dataset loading, at the cost of slower computation.

9. Additional details on Sim2Struct-1000

We constructed our benchmark, Sim2Struct-1000, using the Cryo2Struct dataset, initially containing 7,600 cryo-EM density maps paired with corresponding PDB structures [14]. We specifically chose Cryo2Struct over databases such as AlphaFold DB because each PDB structure is paired with an experimentally determined cryo-EM map, thereby avoiding potential issues associated with synthetic proteins,

¹<https://github.com/ml-struct-bio/cryodrgn>

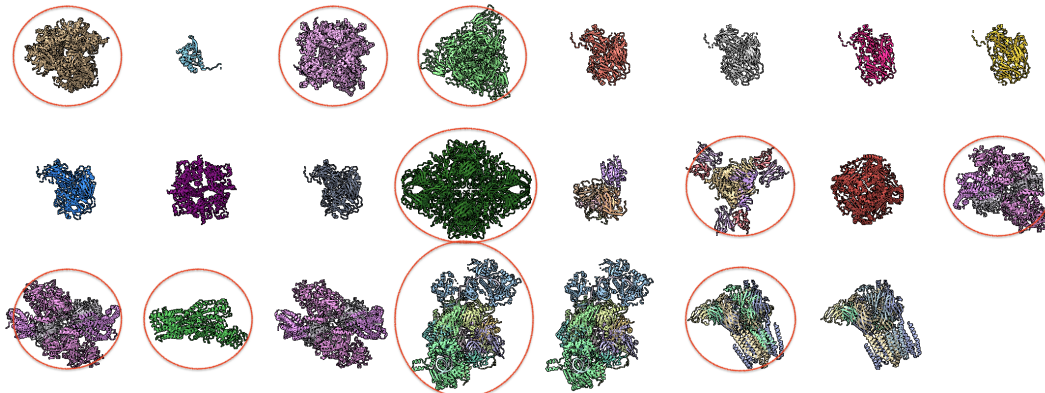


Figure 7. **Qualitative results of Sim2Struct-1000 filtering.** Examples of PDB structures from the Cryo2Struct dataset [14], highlighting those selected (circled) after filtering based on size and structural distinctiveness.

such as disordered regions complicating downstream structure determination [1].

We filtered the initial dataset based on the axis-aligned bounding box dimensions of each PDB structure, retaining only those whose maximum side length fell within the interval [88, 118). This interval ensures each protein comfortably fits within a 256-pixel reconstruction grid, approximately double the protein’s maximal length, to accommodate translations within a ± 20 -pixel range during image projection. This step was critical, as overly small proteins lacked distinctive structural features at our target resolution and too-large proteins would be truncated during image projection. After filtering, we further refined the dataset by eliminating near-duplicate structures, retaining only the first instance of structures sharing identical initial three-character prefixes from their four-character PDB identifiers (e.g. retaining `6cs3.pdb` out of `6cs3.pdb`, `6cs4.pdb`, `6cs5.pdb`, etc.). Figure 7 illustrates the filtering process. From the resulting structures, we selected the first 500 for further processing, subsequently creating smaller subsets (10, 100, and 200 structures) to evaluate model performance at varying dataset scales.

Each retained PDB structure was centered by translating the atomic coordinates to place the geometric centroid at the origin. Next, standardized density maps were generated using the `molmap` command in ChimeraX with parameters set at 3 Å resolution, 1.5 Å grid spacing, and a 256-pixel box size. Although the Cryo2Struct dataset included original EMDB maps, variations in their resolution (ranging 1–4 Å) and box dimensions prompted us to generate standardized synthetic volumes to ensure downstream data consistency [14].

From these standardized volumes, we simulated cryo-EM images by generating 1000 projections per structure, applying a contrast transfer function (CTF), introducing noise corresponding to an SNR of 0.01, and downsampling

images to 128×128 pixels. The final standardized images have dimensions of 128 pixels, 6 Å resolution, and pixel size of 3 Å.

Future work includes evaluating additional protein structure databases to determine their suitability for simulating cryo-EM datasets, particularly to facilitate the development of more generalizable and large-scale cryo-EM reconstruction methods. We plan to release our dataset upon publication on Zenodo with the CC-BY license.

10. Volume metrics for heterogeneous reconstruction

Per-Image FSC We use *per-image FSC* to jointly assess heterogeneity and reconstruction quality following [22]. In cryo-EM, using the Fourier Shell Correlation (FSC) curve is a standard technique for comparing two volumes. The FSC curve calculates the correlation between two volumes (e.g. a reconstructed volume and a ground truth volume) across spherically averaged radial shells in the Fourier domain. Cryo-EM reconstruction methods often reconstruct a volume from a single input image. *Per-image FSC* evaluates the heterogeneous reconstruction quality of a method by computing the FSC between these per-image reconstructions and ground truth volumes. As in [22], to compute the per-image FSC we sample one image per conformation to assess the distribution of reconstructions and compute the area under the FSC curve as a summary statistic.

Figures 8 and 9 provide *per-image FSC* curves for each method across all synthetic datasets. The averaged FSC curves for CryoDRGN and CryoHype on the Tomotwin-100 and all subsets of the Sim2Struct-1000 dataset are presented in Figure 4 and summarized in Table 2.

Additional Volume Metrics To assess the quality of reconstructed volumes against ground truth volumes, we pro-

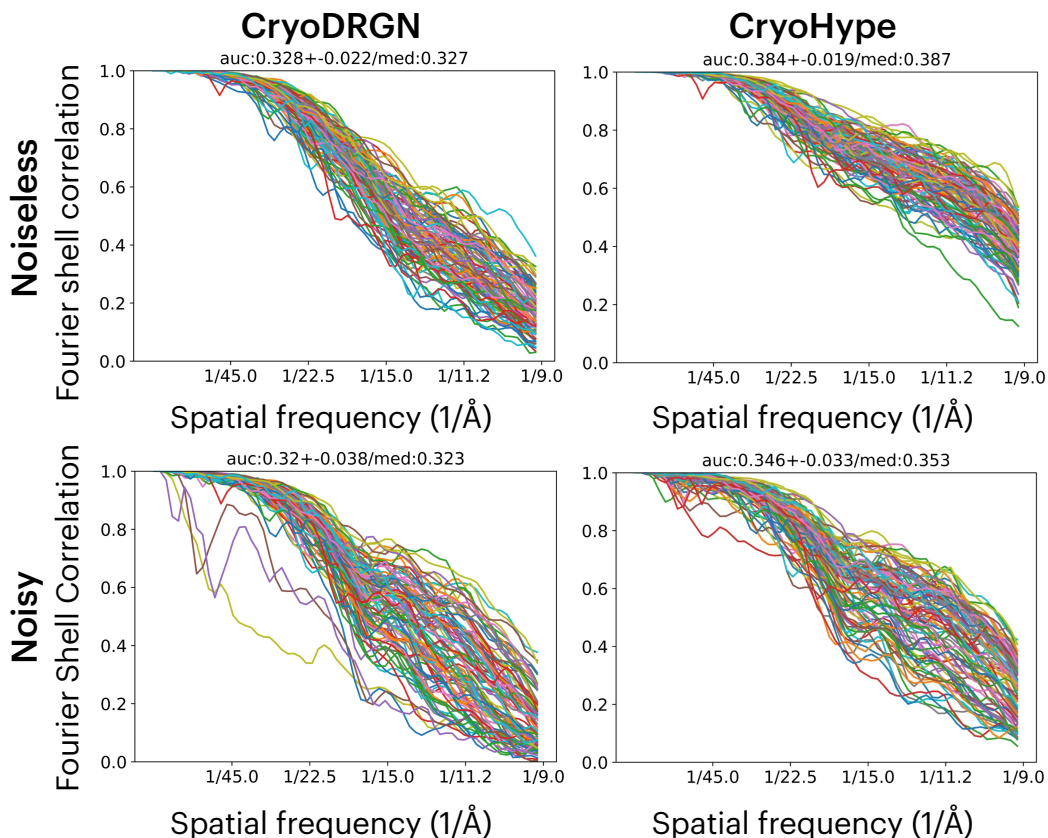


Figure 8. Per-Image FSC curves for Tomotwin-100.

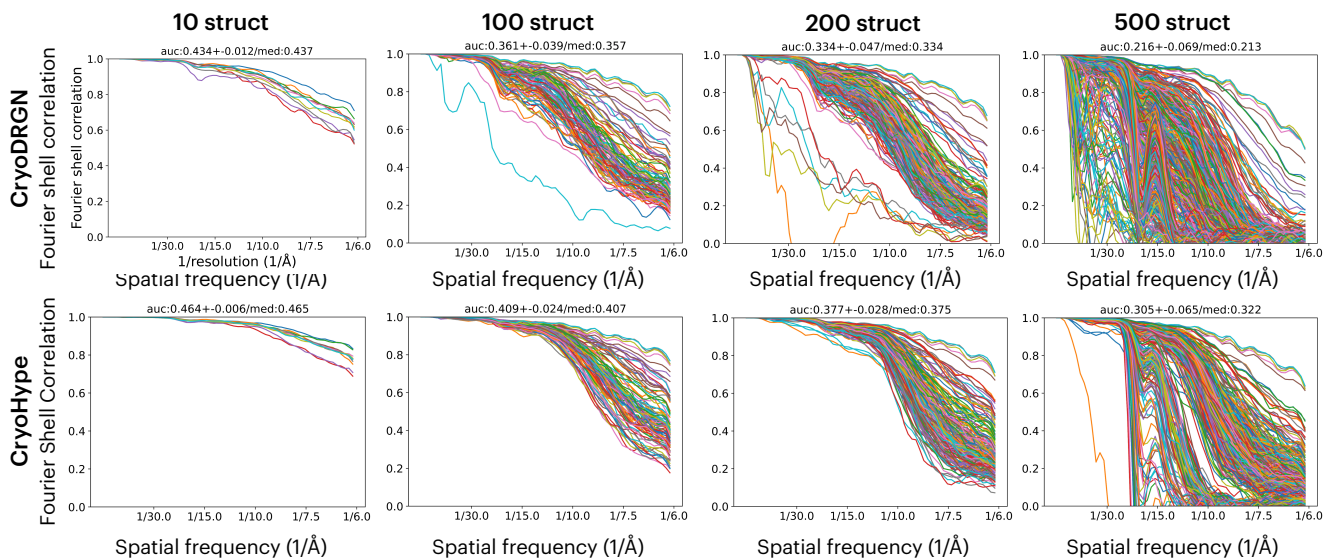


Figure 9. Per-Image FSC curves for the 10, 100, 200, and 500 structure subsets of Sim2Struct-1000

pose the usage of two new metrics, volumetric IoU and Chamfer distance. *Volumetric IoU* (vIoU) is defined as the intersection of the ground truth and predicted volume di-

vided by their union. Higher vIoU values indicate better alignment between the predicted and ground truth volumes. We evaluate shape accuracy using *Chamfer Distance* (CD),

Table 5. Ablation study on CryoHype examining the two main components of the model, evaluated by Chamfer distance and volumetric IoU.

Method	Tomotwin-100			
	↓ CD (std)	Med	↑ vIoU (std)	Med
Concatenation	7.157 (11.300)	2.725	0.487 (0.198)	0.556
U-Net encoder	5.154 (2.360)	4.549	0.451 (0.081)	0.455
CryoHype	2.185 (0.462)	2.111	0.615 (0.061)	0.621

Table 6. Comparison of CryoHype vs different-sized variants of CryoDRGN [58] on the Tomotwin-100 dataset, evaluated using AUC-FSC.

Method	Params	Tomotwin-100	
		Mean (std)	Med
CryoDRGN (base)	20M	0.316 (0.046)	0.321
CryoDRGN (6 layer encoder)	21M	0.316 (0.040)	0.322
CryoDRGN (8 layer encoder)	23M	0.319 (0.038)	0.321
CryoDRGN (6 layer decoder)	21M	0.324 (0.040)	0.328
CryoDRGN (8 layer decoder)	23M	0.324 (0.041)	0.330
CryoDRGN (encoder dim 4096, decoder dim 4096)	155M	0.338 (0.027)	0.340
CryoHype	50M	0.346 (0.033)	0.353

a metric commonly used for assessing the quality of point cloud reconstructions. CD measures the average bidirectional distance between points in the ground truth and predicted point clouds. Lower CD values indicate more accurate reconstructions. Together, these two metrics provide complementary insights into reconstruction quality by evaluating volumetric overlap and shape precision.

The results in Table 5 demonstrate the impact of CryoHype’s main components on these metrics, demonstrating their ability to capture insights on performance. Figure 10 validates these two metrics on the IgG-1D dataset, a dataset modeling a 1D circular motion of one of the fragment antibody (Fab) domains of the human immunoglobulin G (IgG) protein [22]. Figure 11 highlights metric sensitivity to dataset-specific structural characteristics and the increased difficulty posed by more diverse datasets like Sim2Struct-1000. Figure 12 shows the correlation between per-image FSC and our proposed metrics.

Density Threshold Selection To determine which voxels constitute the foreground (object) versus the background in volumetric data, we tuned near-optimal density thresholds to 6.0 for predictions on the Tomotwin-100 dataset, 220 for Sim2Struct-1000 predictions, and 5×10^{-5} for all ground truth structures, ensuring consistent voxel segmentation for evaluation. To aid in selecting these thresholds, we opened the figures in ChimeraX [37] to visually assess and refine the isosurface settings. Final levels were chosen to maximize the completeness of the visualized structures and minimize noisy artifacts.

Thresholding Limitations and Implications A current limitation of our new metrics is that each predicted structure may require individual density level tuning, which limits the ability to draw dataset-wide performance conclusions using these density-dependent metrics. A potential solution to this is to optimize the density level for each predicted structure on a given metric with a greedy search algorithm. Moreover, Chamfer distance is highly sensitive to outliers, resulting in occasional extreme values, particularly at lower density thresholds where noisy or disconnected points are included. Higher density thresholds reduce the number of high-CD outliers but must be carefully tuned to avoid excessive loss of volume and structural details. This sensitivity highlights the importance of selecting density thresholds that balance object completeness with noise reduction.

11. Ablations

In this section, we provide further details on the U-Net ablation experiment done in Section 4.4. Additional quantitative results using our proposed Chamfer distance and volumetric IoU metrics can be found in Table 5. We also provide ablations of different sized CryoDRGN [58] variants vs CryoHype.

U-Net hypernetwork We modify our architecture to only condition the INR decoder by concatenation, turning our network into an autodecoder. We do this by removing all linear heads Head_i except one (see Sec 2.3) and modifying the forward pass of the network to apply the single linear head to just the last output token to produce a latent vector \mathbf{z} , which is used to condition the decoder by

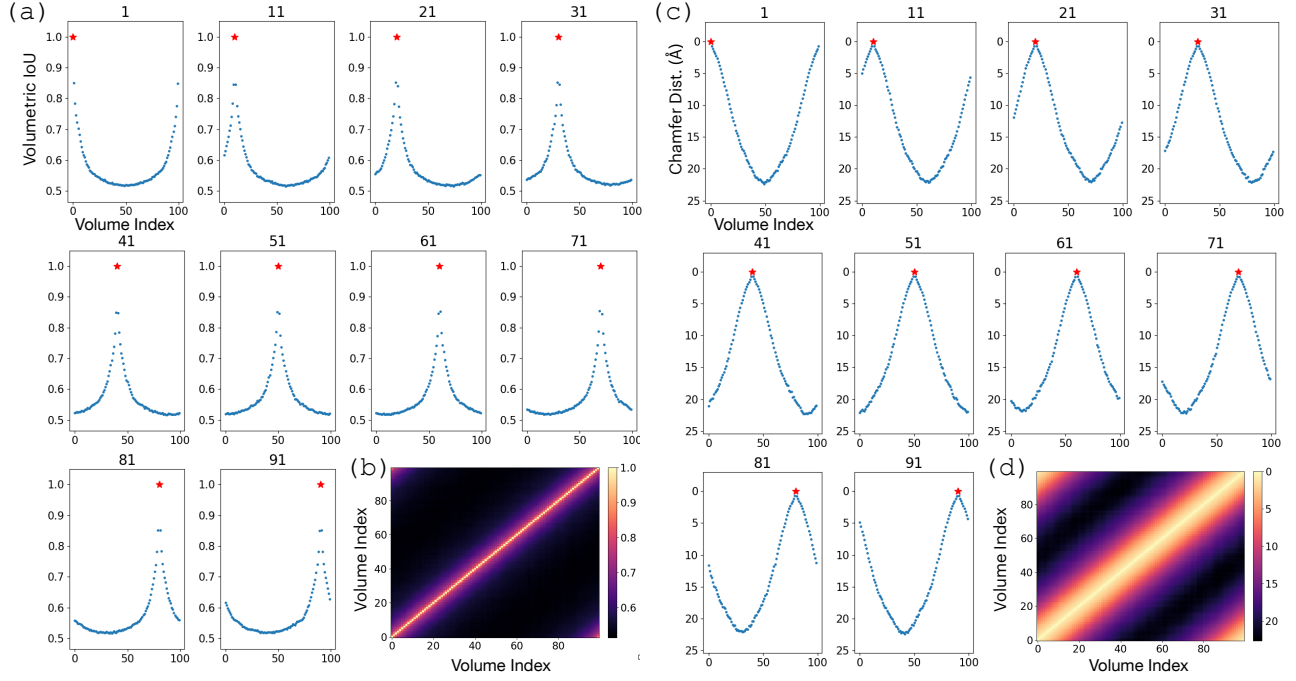


Figure 10. **Dynamic range of CD and vIoU metrics between ground truth volumes for IgG-1D.** (a) Volumetric IoU computed between one reference G.T. structure and all 100 G.T. structures of the IgG-1D dataset. Each plot corresponds to one reference G.T. volume, indicated by the number above the plot and the red star in each plot. Points higher on the y-axis indicate greater structure similarity. (b) Heatmap of vIoU showing the pairwise volumetric IoU for all pairs of G.T. structures. Lighter colors indicate greater structure similarity. Parts (c) and (d) display the corresponding plots for Chamfer distance.

Table 7. CryoHype and cryoDRGN [58] evaluated using traditional FSC metrics on both the Tomotwin-100 dataset and all subsets of the Sim2Struct dataset. Lower is better, with 2 bring the best possible FSC.

Method	Dataset	Structures	FSC at 0.143		FSC at 0.5	
			Mean	Median	Mean	Median
CryoDRGN	Tomotwin-100	100	2.17	2.06	3.14	3.08
CryoHype			2.03	2.00	2.81	2.61
CryoDRGN	Sim2Struct-10	10	2.00	2.00	2.00	2.00
CryoHype			2.00	2.00	2.00	2.00
CryoDRGN	Sim2Struct-100	100	2.01	2.00	2.73	2.75
CryoHype			2.00	2.00	2.30	2.29
CryoDRGN	Sim2Struct-200	200	2.18	2.01	3.09	2.91
CryoHype			2.01	2.00	2.63	2.72
CryoDRGN	Sim2Struct-500	500	3.96	3.37	5.93	4.74
CryoHype			2.68	2.29	3.49	3.20
CryoDRGN	Sim2Struct-1000	1000	6.45	6.10	9.31	6.74
CryoHype			3.87	3.76	4.53	4.57

concatenation. The U-Net [5, 44] encoder for the U-Net ablation takes as input images of shape $[1, D, D]$ and has output shape $[L, D, D]$, where L is the number of layers of the INR and $D = 256$ is a multiple of one of the dimensions of the INR’s weight matrices and initial features

size 144. Since our input originally has shape $[1, 129, 129]$, we reshape the input to size $[1, D, D]$ using interpolation with nearest upsampling. We then apply each linear head $\text{Head}_i, 1 \leq i \leq L$ to a channel of the output, transforming D to the correct size for the given layer. We then repeat the

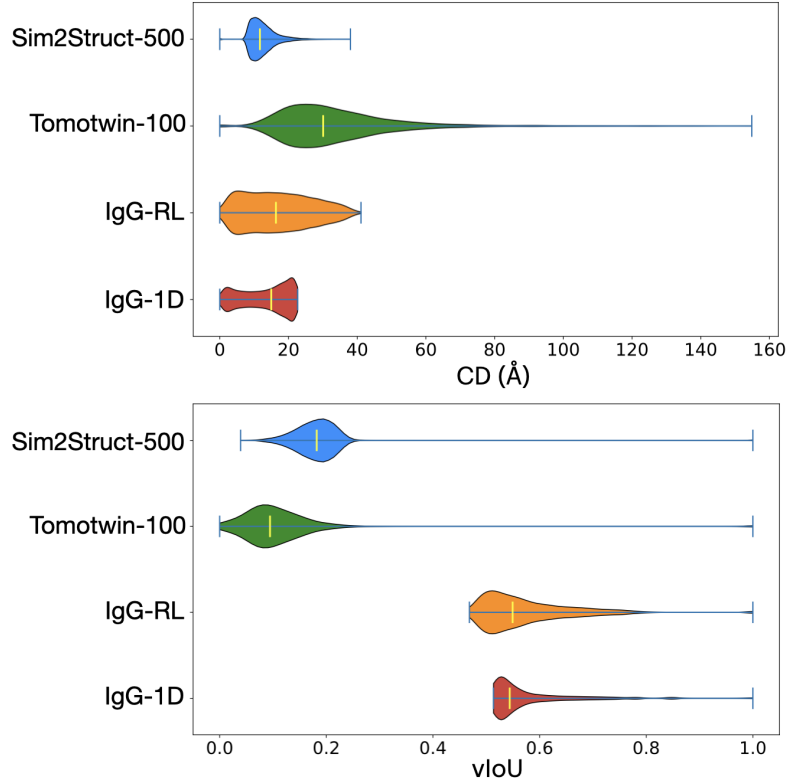


Figure 11. **Dynamic range of CD and vIoU metrics between ground truth volumes for each dataset.** Violin plots show the distribution of Chamfer distance (CD) and volumetric IoU (vIoU) metrics on all G.T. structures for four datasets: Sim2Struct-1000, Tomotwin-100, IgG-RL, and IgG-1D. Lower CD and higher vIoU indicate better shape and volume similarity. Sim2Struct-1000 and Tomotwin-100 exhibit wider variation due to greater structural diversity, while IgG-1D shows the most compact distributions, reflecting its homogeneity.

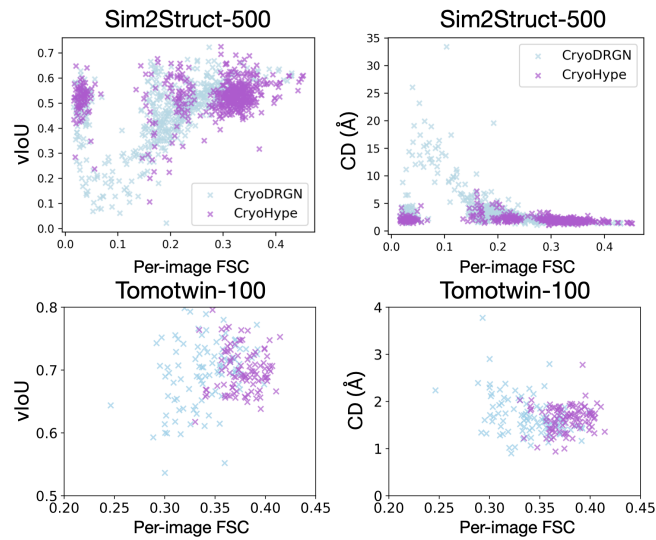


Figure 12. **Quantitative Metric Comparison for Tomotwin-100 and Sim2Struct-1000.** Higher FSC values positively correlate with vIoU and negatively correlate with CD, reflecting improved reconstruction accuracy. CryoHype (purple) outperforms CryoDRGN (blue) across both datasets.

Table 8. CryoHype and cryoDRGN [58] evaluated using supervised classification metrics on all subsets of the Sim2Struct dataset.

Method	Dataset	Structures	Accuracy	Precision	Recall	F1
CryoDRGN CryoHype	Sim2Struct-10	10	0.9998 0.9999	0.9998 0.9999	0.9998 0.9999	0.9998 0.9999
CryoDRGN CryoHype	Sim2Struct-100	100	0.9621 0.9506	0.9523 0.9421	0.9621 0.9506	0.9555 0.9451
CryoDRGN CryoHype	Sim2Struct-200	200	0.9397 0.9632	0.9298 0.9557	0.9397 0.9632	0.9311 0.9581
CryoDRGN CryoHype	Sim2Struct-500	500	0.8375 0.9719	0.8202 0.9635	0.8375 0.9719	0.8166 0.9663
CryoDRGN CryoHype	Sim2Struct-1000	1000	0.6792 0.9753	0.6508 0.9713	0.6792 0.9753	0.6468 0.9724

other dimension as necessary to get the full correct shape. The rest of training is unchanged.

MLP hypernetwork We base our MLP hypernetwork architecture on that of Light Field Networks [52], which uses a separate MLP encoder to generate the weights of each layer. We adapt the architecture of [52] to produce weight tokens instead of directly producing the weights, leaving the rest of the architecture unchanged from the ViT hypernetwork (see Section 2).

Larger CryoDRGN variants The base CryoHype model requires more parameters than the base CryoDRGN model (50M vs 20M). In this ablation study, we show that scaling CryoDRGN does not allow it to match the performance of CryoHype. Quantitative results on the Tomotwin-100 dataset can be found in Table 6. While the performance of CryoDRGN increases with increasing encoder and decoder capacity, the performance of CryoDRGN increases only very gradually, showing that CryoHype scales much better than CryoDRGN. The largest CryoDRGN variant still shows lower performance than the base CryoHype model on Tomotwin-100 (see Table 2), despite having 3 times the number of parameters (155M to 50M).

12. Additional Quantitative Results

In this section, we provide additional quantitative evaluations of our method.

12.1. Traditional FSC

In Table 7, we evaluate CryoHype vs CryoDRGN [58] using the traditional FSC at 0.143 and FSC at 0.5 metrics on both the Tomotwin-100 and all Sim2Struct datasets. We find that, in line with our other quantitative metrics, the performance of CryoHype matches or exceeds the performance of CryoDRGN on all datasets, with CryoHype performing better as the degree of compositional heterogeneity, as measured

by the number of distinct structures, gets more and more extreme.

12.2. Supervised Classification Metrics

Since CryoHype was evaluated quantitatively on synthetic datasets in the fixed-pose setting where the particle poses are known, it also makes sense to evaluate the performance of CryoHype using supervised classification evaluation metrics. We find that overall, CryoHype outperforms cryoDRGN in supervised classification metrics. CryoHype maintains close to perfect classification metrics regardless of the number of structures, whereas cryoDRGN’s performance is close to perfect at 10 and 100 structures, being to drop at 200 structures, and degrades rapidly as the number of structures increases, mirroring the trends observed in the other metrics (AUC-FSC, CD, vIoU). The large drops at 500 and 1000 structures are also reflected in the latent space, with the poor quantitative classification metrics for cryoDRGN reflected as increasingly poor organization at the center of the latent space (see Figure 5).

12.3. Additional baselines

In this section, we report the results of traditional maximum likelihood classification methods with fixed pose (e.g. cryoSPARC 3D classification [40]) on our new Sim2Struct dataset. Quantitative results can be found in Table 9. As with the cryoSPARC results reported in our paper (originally from CryoBench [22], see Table 2), we confirm that cryoSPARC’s 3D classification method struggles with compositional heterogeneity and especially the extreme compositional heterogeneity considered in our paper. In particular, the results on the 100 structure subset of Sim2Struct mirror that of Tomotwin-100. At even more extreme levels of heterogeneity (>100 classes), we find that cryoSPARC 3D classification throws an error.

Table 9. Performance of cryoSPARC’s fixed pose 3D classification method on the Sim2Struct dataset, evaluated using AUC-FSC.

Method	Dataset	AUC-FSC	
		Mean (std)	Med
cryoSPARC 3D class (fixed pose)	Sim2Struct-10	0.204 (0.036)	0.224
cryoSPARC 3D class (fixed pose)	Sim2Struct-100	0.071 (0.055)	0.037

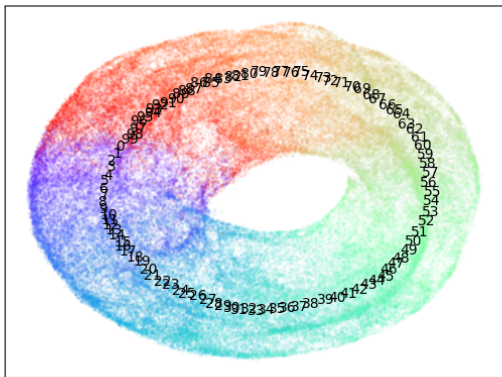


Figure 13. **IgG-1D latent space** We find that CryoHype successfully captures the 1D circular motion of the IgG-1D dataset.

13. Conformational Heterogeneity

Although CryoHype was not designed to target conformational heterogeneity, it is still able to recover conformational heterogeneity. When tested on the IgG-1D dataset [22], CryoHype successfully recovers the circular motion that characterizes the dataset (see Fig. 13) when augmented with an additional smoothness loss.

14. Additional Qualitative Results

In this section, we provide additional examples of reconstructed volumes for both CryoHype and CryoDRGN on each dataset.

Figures 14 and 15 show groundtruth, CryoHype, and CryoDRGN reconstructions for the Tomotwin-100 and Sim2Struct-1000, respectively. We see that overall, CryoHype is both able to reconstruct some shapes that CryoDRGN cannot. In particular, it seems that CryoDRGN struggles with proteins with loops, while CryoHype does a better job of reconstructing these proteins. Additionally, CryoHype generally has higher resolution and preserves fine details better than CryoDRGN.

Figure 16 shows reconstructed volumes for each class of EMPIAR-10076. Each CryoHype structure is generated by randomly sampling from latent encoding of particles with the corresponding class assignments from [10].

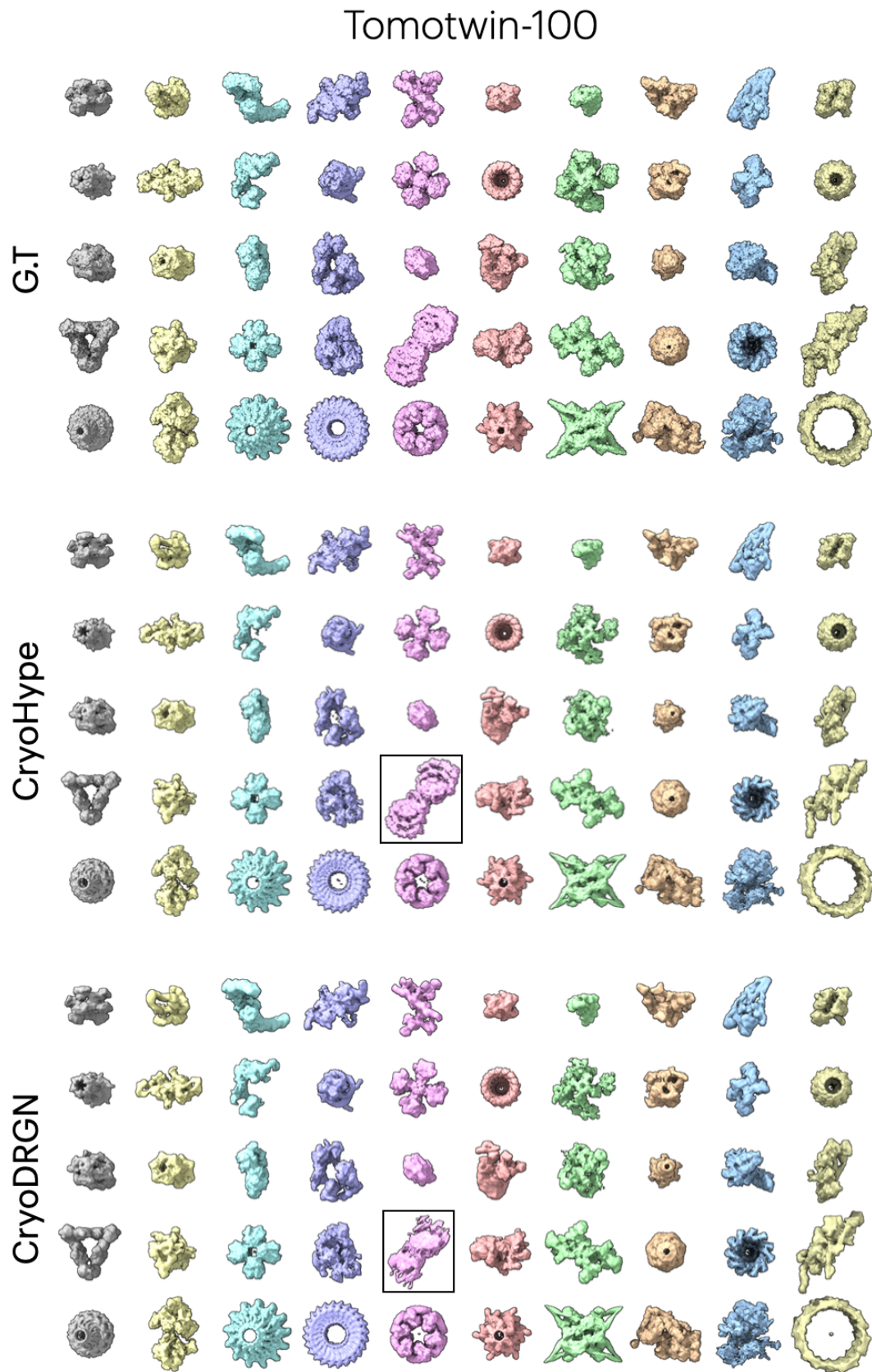


Figure 14. **Tomotwin-100 (SNR 0.01) qualitative results** Last 50 volumes reconstructed by CryoHype and CryoDRGN for the Tomotwin-100 dataset.

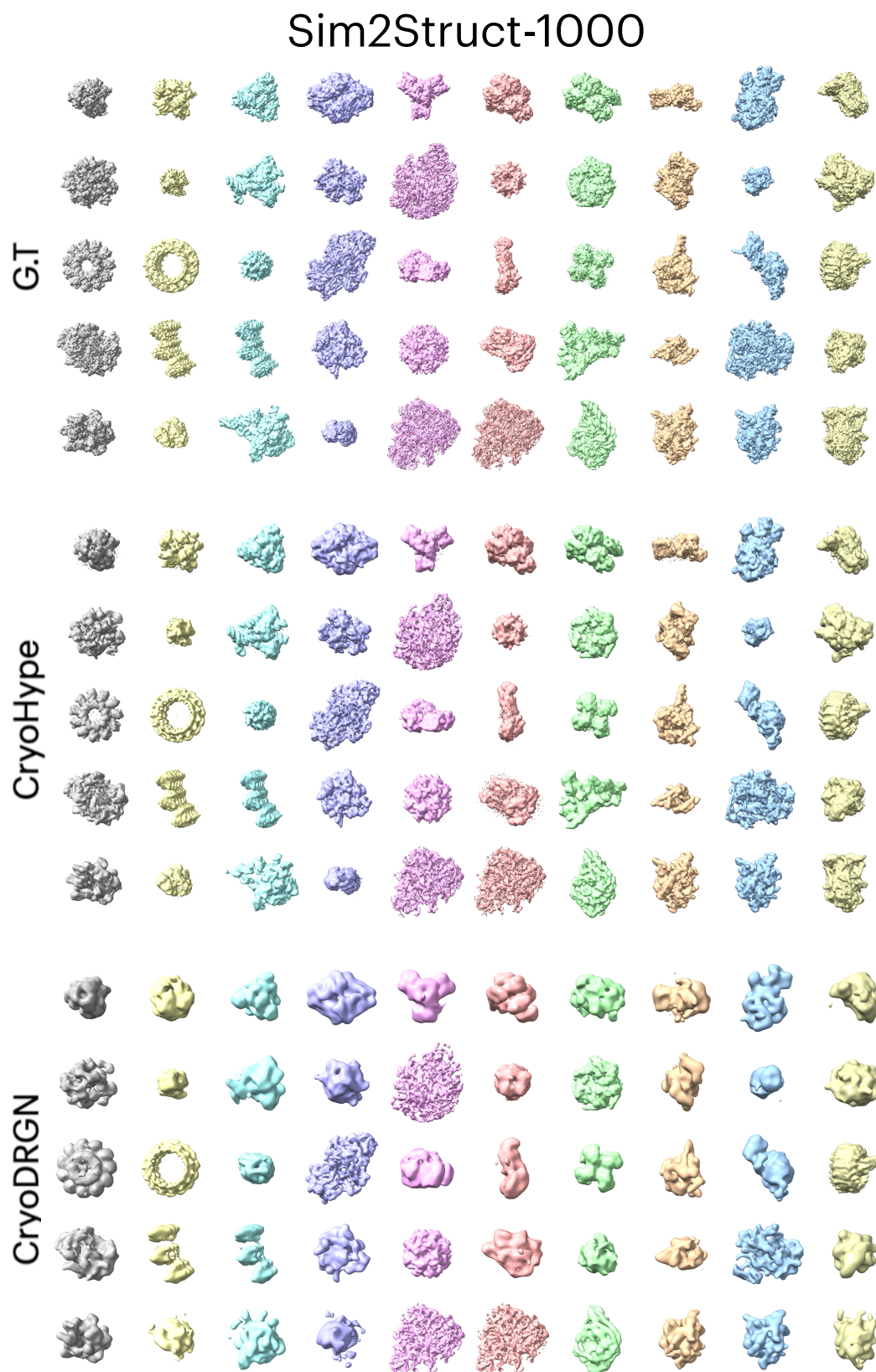


Figure 15. **Sim2Struct-1000 qualitative results with G.T** Last 50 volumes reconstructed by CryoHype and CryoDRGN for the Sim2Struct-1000 dataset.

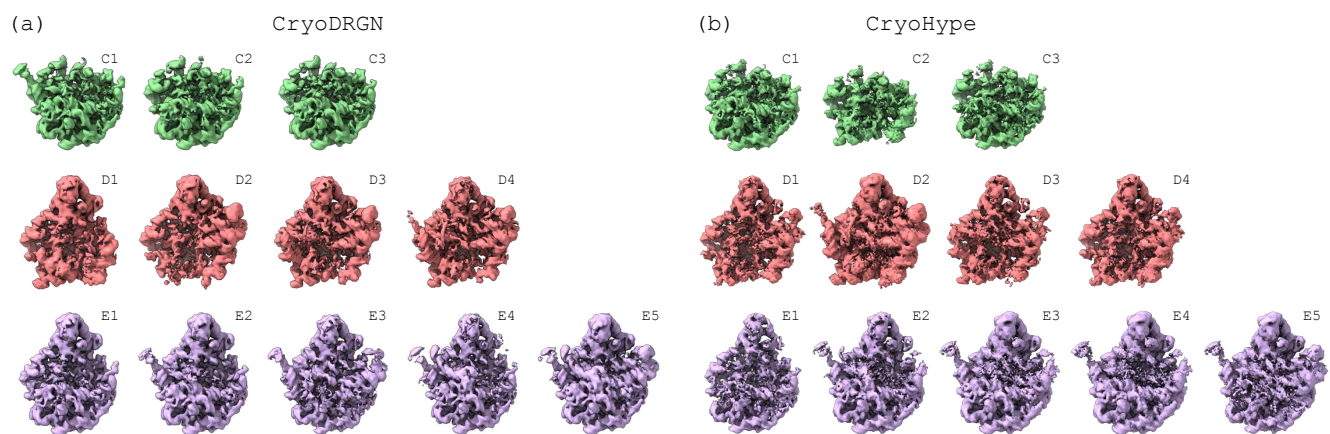


Figure 16. **EMPIAR-10076** Reconstructed volumes of ribosome assembly minor classes for (a) CryoDRGN and (b) CryoHype.